# Investigation of ultrasonic backscatter using three-dimensional finite element simulations

Yuan Liu, Anton Van Pamel, Peter B. Nagy, and Peter Cawley

Citation: The Journal of the Acoustical Society of America **145**, 1584 (2019); doi: 10.1121/1.5094783
View online: https://doi.org/10.1121/1.5094783
View Table of Contents: https://asa.scitation.org/toc/jas/145/3
Published by the Acoustical Society of America

**ARTICLES YOU MAY BE INTERESTED IN**

Investigation of the repeatability and reproducibility of hydrophone measurements of medical ultrasound fields
The Journal of the Acoustical Society of America **145**, 1270 (2019); https://doi.org/10.1121/1.5093306

Generalized optical theorem for an arbitrary incident field
The Journal of the Acoustical Society of America **145**, EL185 (2019); https://doi.org/10.1121/1.5092581

Large acoustoelastic effect for Lamb waves propagating in an incompressible elastic plate
The Journal of the Acoustical Society of America **145**, 1221 (2019); https://doi.org/10.1121/1.5092604

Effective property evaluation and analysis of three-dimensional periodic lattices and composites through Bloch-wave homogenization
The Journal of the Acoustical Society of America **145**, 1259 (2019); https://doi.org/10.1121/1.5091690

Superdirective beamforming applied to SWellEx96 horizontal arrays data for source localization
The Journal of the Acoustical Society of America **145**, EL179 (2019); https://doi.org/10.1121/1.5092580

Investigation on the diffusive surface modeling detail in geometrical acoustics based simulations
The Journal of the Acoustical Society of America **145**, EL215 (2019); https://doi.org/10.1121/1.5092821



# Investigation of ultrasonic backscatter using three-dimensional finite element simulations

Yuan Liu,[1,a)] Anton Van Pamel,[1] Peter B. Nagy,[2,b)] and Peter Cawley[1]
[1]*Department of Mechanical Engineering, Imperial College London, Exhibition Road, London, SW7 2AZ, United Kingdom*
[2]*Department of Aerospace Engineering and Engineering Mechanics, University of Cincinnati, 2600 Clifton Avenue, Cincinnati, Ohio 45221, USA*

(Received 18 December 2018; revised 16 February 2019; accepted 4 March 2019; published online 27 March 2019)

Theoretical models are commonly used to describe ultrasonic backscattering in polycrystalline materials. However, although a full multiple scattering formalism has been derived, due to the difficulty in evaluation, currently only the single and double scattering effects have been evaluated. Three-dimensional finite element (3D FE) models have recently been demonstrated to be capable of predicting ultrasonic attenuation in polycrystalline materials and thereby show great potential in overcoming this limitation. In this paper, the application of 3D FE models is extended to the backscatter problem. First, longitudinal-to-longitudinal backscattering amplitudes from single grains are predicted, where the setup and configuration of the finite element (FE) model are verified with an isotropic spherical inclusion for which an exact solution is available. Subsequently, backscatter in terms of the root-mean-square noise levels in two different pulse-echo scenarios is investigated; the first is an idealised configuration with plane wave transmission and point reception; the second represents a more realistic finite-size transducer acting with the same apodization in both transmission and reception. Comparisons of FE predictions and approximate theoretical solutions within a range of validity show good agreement; however, the results demonstrate that 3D FE is useful where the simple Independent Scatterer models break down. As computing power increases, 3D FE is an increasingly viable tool to further the understanding of wave propagation in polycrystalline materials.
*© 2019 Author(s). All article content, except where otherwise noted, is licensed under a Creative Commons Attribution (CC BY) license (http://creativecommons.org/licenses/by/4.0/).*
https://doi.org/10.1121/1.5094783

[MRH] Pages: 1584–1595

## I. INTRODUCTION

Ultrasound locates and characterises defects in a material by the scattering of waves from the defects, which is shown as echoes in the received signals. Similarly, the ultrasound waves can also be scattered from the grain/colony boundaries in polycrystalline materials due to the acoustic impedance contrast caused by different alignments of principal axes of the grains/colonies (Mech *et al.*, 1977). The grain boundary scattering causes two phenomena: attenuation of the coherent waves and microstructural noise. Good understanding of the two phenomena is important for Non-Destructive Evaluation (NDE) inspection and material characterisation of polycrystalline materials. The first phenomenon, scattering induced attenuation has been widely researched (Stanke, 1985; Stanke and Kino, 1984; Yang and Rokhlin, 2012) and in recent years, various approaches, e.g., Weaver (1990), and extensions to more complicated microstructures (Ahmed and Thompson, 1996; Turner, 1999; Yang *et al.*, 2011; Yang and Rokhlin, 2013) have been investigated. In addition to the theoretical models, the finite element method has been proposed as an approach for the study of attenuation (Chassignole *et al.*, 2009; Feuilly *et al.*, 2009). Our group has achieved the first realistic three-dimensional (3D) simulation of wave propagation in polycrystals with a highly efficient GPU based solver POGO (Huthwaite, 2014), with which scattering induced attenuation in different regimes has been predicted. Systematic studies on various ingredients of the simulations, such as the meshing, the representation of grains, the description of grain statistics, randomising of crystal orientations, understanding of choices of boundary conditions and verification of correct propagation in anisotropic crystals, have been carried out and reported in several preceding papers (Van Pamel *et al.*, 2015; Van Pamel *et al.*, 2016; Van Pamel *et al.*, 2018; Van Pamel *et al.*, 2017). Recently, another group has also achieved realistic 3D simulations with a commercial finite element (FE) software PZFLEX, a study on the influence of grain morphology on attenuation in polycrystalline materials being carried out (Ryzy *et al.*, 2018).

Backscattered ultrasonic grain noise, another phenomenon caused by the scattering, has also attracted much interest in the past decades. The Independent Scatterer Model (ISM), which predicts absolute noise levels, was developed and validated with experiments (Margetan *et al.*, 1991; Margetan *et al.*, 1994). This model accounts for system effects by adopting the Thompson and Gray (1983) model and for the material by a characteristic material parameter, termed the

a)Electronic mail: y.liu14@imperial.ac.uk
b)Also at: Department of Mechanical Engineering, Imperial College London, Exhibition Road, London, SW7 2AZ, United Kingdom.

 ©Author(s) 2019.

figure of merit (FOM). The FOM is identical to the square root of the backscattering coefficient used in Rose (1991, 1992, 1993), which relates the backscattered ultrasonic noise to the microstructure and has been experimentally validated (Thompson *et al.*, 1992). More recently, another theoretical model of single scattering response in polycrystalline materials for longitudinal-to-longitudinal (L-L) scattering was evaluated (Ghoshal *et al.*, 2007), being able to capture the overall behaviour observed in Margetan *et al.* (1991). The model was then extended to include ultrasonic wave propagation through a fluid-solid interface and experimentally validated (Ghoshal and Turner, 2010). Following a similar formalism, models describing longitudinal-to-transverse scattering (Hu *et al.*, 2013) and transverse-to-transverse scattering (Hu and Turner, 2017) have been developed. Based on these models, research has been carried out to study materials with more complicated microstructures (Arguelles *et al.*, 2016; Han and Thompson, 1997; Lobkis *et al.*, 2012; Yang and Rokhlin, 2013).

Most of the noise models established in these studies are based on a single scattering assumption, which assumes the reflection from one grain is not affected by other grains. This assumption limits the validity of the models to weakly scattering regimes because the interaction between grains is not negligible if the scattering is high (Margetan *et al.*, 2005). To estimate the range of the validity, based on a multiple scattering framework (Ghoshal *et al.*, 2007), the double scattering effect has been derived and evaluated in Hu and Turner (2015), the results of which allow the uncertainty of the single scattering approximation to be determined and show the potential of solving highly scattering problems. However, significant difficulties remain to develop a theoretical ultrasonic backscattering model which includes the full multiple scattering events. Apart from the theoretical methods, FE modelling is an alternative approach to study the noise behaviour. Unlike the theoretical models, the FE modelling is capable of solving the scattering problem without major simplifying assumptions, which makes it a promising tool to give an accurate prediction of grain noise in both weakly and highly scattering regimes. Until recently, computational costs have limited FE simulations to two-dimensional (2D) (Bai *et al.*, 2018; Ghoshal and Turner, 2009). Even though it has shown that some representative features of the 3D ultrasonic scattering can be captured by the 2D model, 3D simulation remains necessary to investigate the grain noise behaviour due to the inherent 3D nature of the physical phenomenon.

The recent 3D simulations have predicted realistic attenuation and wave speed dispersion (Van Pamel *et al.*, 2015; Van Pamel *et al.*, 2016; Van Pamel *et al.*, 2018; Van Pamel *et al.*, 2017), but have not yet been used for backscatter. This paper makes use of this proven capability to a new and important application: realistic 3D simulations of backscatter. Initially, a FE model which considers the scattering response from grains on an individual basis is developed and the measured backscattering amplitudes are compared to the theoretical predictions of the established theories. Then a FE model with the entire aggregate of grains is considered with two transmit-receive configurations, one with a plane wave excitation and incoherent average of the received signals and another one with a finite transducer and coherent average of the received signals. The root-mean-square (rms) noise levels of both configurations are compared with the theoretical solutions developed following the derivation of the ISM in Margetan *et al.* (1993). The contribution of shear waves and multiple scattering and the effect of the coherent attenuation on the grain noise are discussed.

## II. PREDICTION OF BACKSCATTERING AMPLITUDE FROM SINGLE INCLUSIONS IN AN ISOTROPIC HOST MATERIAL

Before using the three-dimensional finite element (3D FE) approach to study the grain noise, which is a result of the scattering from an aggregate of grains, it is important to show that this approach can accurately predict the scattering response from a single grain. The theoretical models to describe the L-L scattering of a plane wave by an inclusion in an isotropic host material have been well established; for example, the exact solution for an isotropic spherical inclusion has been given in Ying and Truell (1956), and a more general solution applicable to a small weakly-scattering inclusion, shown in Gubernatis *et al.* (1977) and Schmerr and Song (2007) has been developed based on the Born approximation. This enables the implementation of the FE model for this study to be verified on a known problem for which an established analytical solution is available.

To measure the L-L backscattering amplitude, a "single-grain" FE model, shown in Fig. 1 is developed. This model has dimensions of $10 \times 10 \times 35\,\text{mm}^3$ and contains $85 \times 10^6$ degrees of freedom. It is meshed with uniform hexahedral elements and the inclusion, located on the central axis, is modelled by the aggregate of elements whose material properties are different from those of the medium. The medium made from an isotropic material, of which the Young's

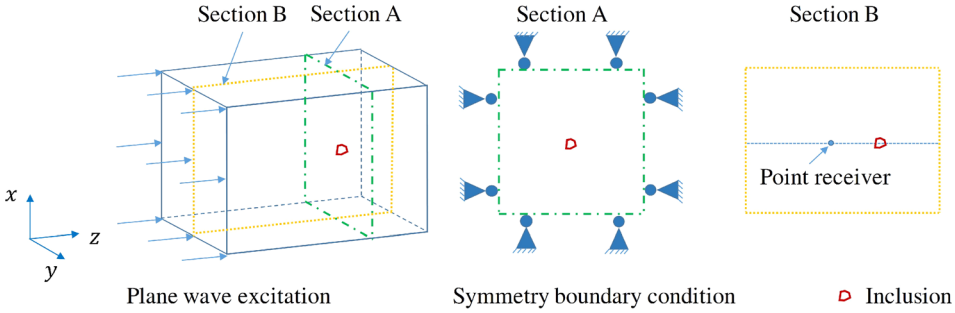



FIG. 1. (Color online) "Single-grain" model ($10 \times 10 \times 35\,\text{mm}^3$): an inclusion located at the central axis along the excitation direction in an isotropic host material is subject to a plane wave excitation. A point receiver used to capture the first backscattered longitudinal reflection from the inclusion is located on the central axis.

modulus, Poisson's ratio and density are 214 GPa, 0.3 and 8000 kg/m$^3$, respectively, will be used in all the cases discussed in this section. Symmetry boundary conditions are used on the model surfaces parallel to the $z$-axis, which mirror the model on the boundaries so effectively generate an infinitely wide model with repeating grain structures. All the nodes on one of the model surfaces in the $x$–$y$ plane, which is indicated by the blue arrows in Fig. 1, are used as transmitters, with which a plane wave propagating in the $z$-direction is effectively generated. The centre frequency of the excitation considered in this section is in the range from 2 to 6 MHz. As the longitudinal velocity of the host material is 6000 m/s, compromising between accuracy and efficiency (Drozdz, 2008), the element edge length is set as 0.05 mm, so there are at least 20 elements per wavelength. A point receiver located on the central axis is used to capture the first backscattered longitudinal reflection from the inclusion.

When calculating the backscattering amplitude, apart from the amplitude of the reflection from the inclusion, the amplitude of the incident wave illuminating the inclusion is also needed. In addition, as the reflection from the inclusion is relatively small in the following cases, the noise caused by numerical error cannot be ignored. Therefore, another FE model, which is referred to as the reference model, is developed with the same properties and dimensions but without the inclusion. Two point receivers, one at the same location as the centre of the inclusion in the "single-grain" model and the other at the same location as that of the receiver in the "single-grain" model, are used to capture the incident wave arriving at the position of the inclusion and a reference signal which can be used to remove the numerical error from the raw signal obtained with the "single-grain" model, thereby revealing a clear reflection from the inclusion.

We begin with a simple case, an isotropic spherical inclusion, and then consider more complicated cases, such as an inclusion with anisotropic material properties or an irregular shape. It is assumed that in all cases, there is no variation in density from the inclusion to the medium, in which case the L-L scattering amplitude in the Born approximation can be written as (Rose, 1992)

$$A = -\frac{\Delta C_{ijkl}}{4\pi\rho v^2}\int \gamma(\mathbf{y}) u^0_{i,j} u^0_{k,l}\, \mathrm{d}V, \tag{1}$$

where $\Delta C_{ijkl}$ denotes the difference between the elastic constants of the inclusion and the medium; $i$, $j$, $k$, $l$ indicate the directions of the 1–2–3 coordinate system; $\rho$ is the density; $v$ is the longitudinal wave speed of the host material; $V$ is the volume of the inclusion; $\gamma(\mathbf{y})$ is defined to be unity if $\mathbf{y}$ is inside of the inclusion and zero otherwise; $\mathbf{u}^0$ is the incident displacement field; repeated subscripts indicate summation, while subscripts following commas indicate derivatives.

If the excitation signal is assumed to be a unit harmonic plane wave propagating in the $z$-direction, which can be expressed as $\mathbf{u}^0 = [0, 0, \mathrm{e}^{\mathrm{j}kz}]$ in the $x$–$y$–$z$ coordinate system (corresponding to the 1–2–3 system), Eq. (1) can be written as

$$A = \frac{k^2 \Delta C_{3333}}{4\pi\rho v^2}\int \gamma(\mathbf{y}) \mathrm{e}^{2\mathrm{j}kz}\, \mathrm{d}V, \tag{2}$$

where $\Delta C_{3333}$, which will be written as $\Delta C_{33}$ in the following text, denotes the difference between the 3333 elastic constant of the inclusion and the medium.

### A. A spherical inclusion

In this section, the backscattering amplitude from an isotropic spherical inclusion under a 4 MHz plane wave excitation is predicted. The radius of the inclusion is 0.31 mm, i.e., 0.2$\lambda$. The Young's modulus, Poisson's ratio, and density of the inclusion are 223 GPa, 0.3, 8000 kg/m$^3$, respectively. The relatively small impedance difference (2%) between the inclusion and the medium is to ensure the validity of the Born approximation, and therefore the accuracy of the theoretical prediction based on that.

By dividing the frequency response of the reflection from the inclusion by that of the incident wave arriving at the inclusion and multiplying it by the distance to account for the spherical divergence of the scattered field, the FE backscattering amplitude can be obtained (Schmerr and Song, 2007). This result is plotted as the red dots in Fig. 2(a), along with the prediction of the theoretical solution based on the Born approximation, shown as the blue curve, and that of the exact solution (Ying and Truell, 1956), shown as the purple curve. The $x$ axis shows the product of the wave number, denoted by $k$, and the radius of the inclusion, denoted by $b$ ($b$ is constant at 0.31 mm in Fig. 2). Good agreement between the three predictions can be seen, verifying the FE simulation for the scattering from an isotropic spherical inclusion. As the staircase mesh approach is relatively slow to converge (Drozdz, 2008), discrepancies can be seen at relatively high $kb$. (There are 24 elements per wavelength at the highest frequency in the range covered in the FE simulation.)

As cubic single-crystal symmetry is considered in this study, it is of great importance to verify the FE simulation for

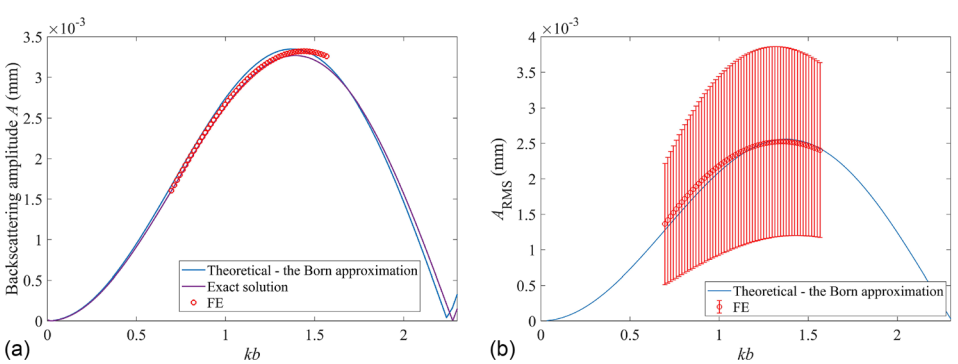



FIG. 2. (Color online) Comparison of FE and theoretical backscattering amplitudes of a spherical inclusion with (a) an isotropic material and (b) a cubic material with a Zener anisotropy factor $[A_z = 2C_{44}/(C_{11} - C_{12})]$ (Lau and McCurdy, 1998) of 1.4. One hundred random orientations for the cubic material are considered. The rms of the 100 FE results are plotted as red dots in (b) and the error bars show their standard deviation.

the scattering from an inclusion with this symmetry. Therefore, we will consider the same spherical inclusion under the same excitation but with a cubic material, of which the Voigt averages are the host material properties given in the beginning of Sec. II. Density and Poisson's ratio are the same as those of the isotropic inclusion, while the elastic constants $C_{11}$, $C_{12}$, and $C_{44}$ are 266.7, 134.1, and 92.9 GPa, respectively. One hundred realisations with random crystallographic orientations of the inclusion are run and the rms of the 100 backscattering amplitudes is shown as the red dots in Fig. 2(b), along with the error bars showing their standard deviation.

The theoretical prediction of the rms backscattering amplitude of the inclusion with random crystallographic orientations can be calculated using Eq. (2), where $\Delta C_{33}$ is replaced by $\sqrt{\langle \triangle C_{33}^2 \rangle}$, which is the rms difference between the 3333 elastic constant of the inclusion, averaged over all grain orientations, and that of the medium. The expression of $\langle \triangle C_{33}^2 \rangle$ for a cubic material is given by Margetan *et al.* (1993)

$$\langle \Delta C_{33}^2 \rangle = \frac{16(C_{11} - C_{12} - 2C_{44})^2}{525}. \tag{3}$$

The theoretically predicted rms backscattering amplitude is plotted as the blue curve in Fig. 2(b), from which good agreement between the FE and theoretical predictions can be seen. A relatively large standard deviation can be seen in the FE results, which shows that the crystallographic orientation of a grain has significant influence on its backscattering amplitude.

### B. An irregular shaped inclusion

So far, the implementation of the 3D FE model has been verified for the scattering from a spherical inclusion. However, the shape of a real grain is usually far more irregular than a sphere. Therefore, we consider an inclusion with an irregular shape, which is more representative of a real grain.

In order to get an inclusion with a representative shape of a real grain, a FE model with an aggregate of grains, which will be referred to as a "multi-grain" model, is generated using Voronoi tessellation (Quey *et al.*, 2011). This "multi-grain" model has the same size as the "single-grain" model and contains 28 000 grains with an average linear dimension of 0.34 mm (the averaged grain volume is 0.125 $mm^3$). Structured meshes, which have been shown to perform well with sufficiently fine discretisation in modelling a grained material (Van Pamel *et al.*, 2015), are used here. The element size (element edge length) needs to meet

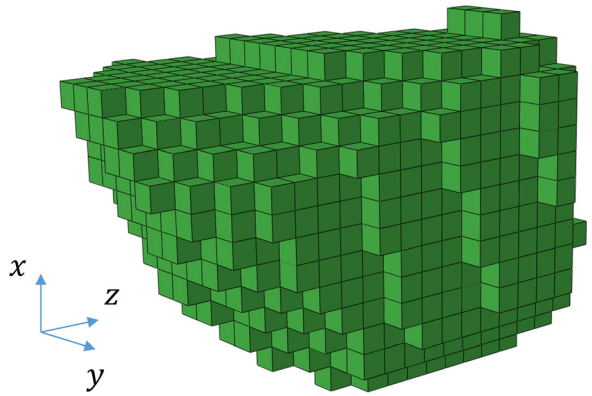



FIG. 3. (Color online) An irregular shaped inclusion modelled with uniform hexahedral elements with an edge length of 0.05 mm.

two requirements, at least ten elements per wavelength (Smith, 1975), and at least ten elements per cubic root of the averaged grain volume (Van Pamel *et al.*, 2015). From the model parameters given above, it can be seen that the element size adopted here is restricted by the latter requirement and therefore, it is set to be 0.05 mm. (As all the "multi-grain" models used in this paper have the same mean grain size, the same element type and size will be adopted in their discretisations.) Using the same discretisation in the "multi-grain" model and the "single-grain" model enables a grain in the "multi-grain" model to be "moved" to the "single-grain" model to represent an inclusion, as shown below.

Then a grain, of which the FE model is shown in Fig. 3, is randomly picked from the "multi-grain" model. Its geometry is used to model the inclusion, replacing the spherical one, in the "single-grain" model. Similarly, we first consider the inclusion with an isotropic material and then a cubic material. The results are shown in Fig. 4, where the $x$ axis shows the product of the wave number $k$ and half of the average linear dimension of the grains in the "multi-grain" model, denoted by $b$ ($b$ is constant at 0.17 mm in Fig. 4). A 4 MHz excitation is used in the FE simulations for the isotropic inclusion and two centre frequencies, 2 and 4 MHz, are used in the FE simulations for the inclusion with cubic symmetry in order to cover a large range of $kb$. Good agreement between the FE and theoretical predictions can be seen for both the isotropic and cubic inclusions. Similar to Fig. 2(b), a large standard deviation can be seen in the FE results, showing the significant influence of the crystallographic orientation of a grain on its backscattering amplitude. As the

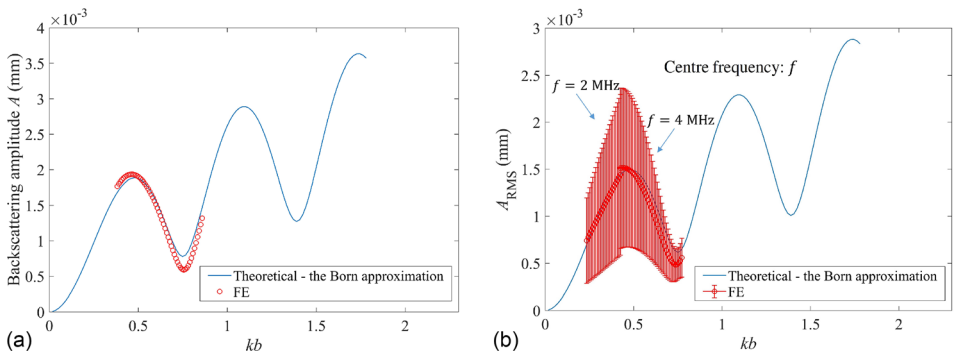



FIG. 4. (Color online) Comparison of FE and theoretical backscattering amplitudes of an irregular inclusion with (a) an isotropic material and (b) a cubic material with a Zener anisotropy factor of 1.4. One hundred random orientations for the cubic material are considered. The rms of the 100 FE results are plotted as red dots in (b) and the error bars show their standard deviation. Two centre frequencies, 2 and 4 MHz, are used in the FE simulations for the inclusion with cubic symmetry.

aim of the comparison is to verify the implementation of the FE model, the material properties of the inclusion and host material are set to ensure a small difference between the impedance of the inclusion (averaged over all orientations) and that of the host material, and hence the validity of the Born approximation. This is the precondition of good agreement seen in Fig. 4. There is no doubt that the Born approximation would break down if the impedance contrast was larger, in which case a discrepancy between the FE and theoretical prediction would be expected.

### C. rms backscattering amplitude of single inclusions with random shapes and material orientations

Up to now, it has been shown that the FE implementation correctly calculates the backscattering of a single grain with an isotropic or a cubic material in a homogeneous isotropic host, for a case that is within the validity of the Born approximation. In this section, a further test will be carried out to assess whether it can give an accurate statistical prediction of the rms backscattering amplitude of single random shaped inclusions.

The theoretical prediction of the rms backscattering amplitude of single grains, which can be regarded as random shaped inclusions, can be written as (Margetan *et al.*, 1993; Rose, 1992, 1993)

$$A_{\mathrm{RMS}} = \frac{\sqrt{\dfrac{\pi^2 f^3 \langle \Delta C_{33}^2 \rangle}{\rho^2 v^7} \displaystyle\int_0^\infty L \sin\left(\frac{4\pi f L}{v}\right) w(L)\mathrm{d}L}}{\sqrt{n_{\mathrm{g}}}}, \tag{4}$$

where $n_{\mathrm{g}}$ is the grain density; $f$ is the frequency; $\rho$ is the density; $v$ is the Voigt averaged longitudinal velocity, for cubic symmetry which is given by

$$v = \sqrt{\frac{3C_{11} + 2C_{12} + 4C_{44}}{5\rho}}, \tag{5}$$

$w(L)$ is the two point correlation function, which shows the probability that two arbitrarily placed points a distance $L$ apart in the specimen are located in the same grain, assuming the model is statistically isotropic and homogeneous. Here, $w(L)$ is obtained by fitting a 4-exponential series to the real correlation function obtained from the "multi-grain" model (Van Pamel *et al.*, 2018).

To predict the rms backscattering amplitude with FE simulations, a number of inclusions which are representative of real grains are needed. The same "multi-grain" model, which is made from the same cubic material used in Secs. II A and II B, with different orientations to different grains, is used here to provide the geometry and material information for inclusion in the "single-grain" model. Five hundred grains are randomly picked from the "multi-grain" model. For each of them, the geometry and material information are used to define the inclusion, which is at the central axis in the "single-grain" model, as shown in Fig. 1, and the backscattering amplitude from it is calculated.

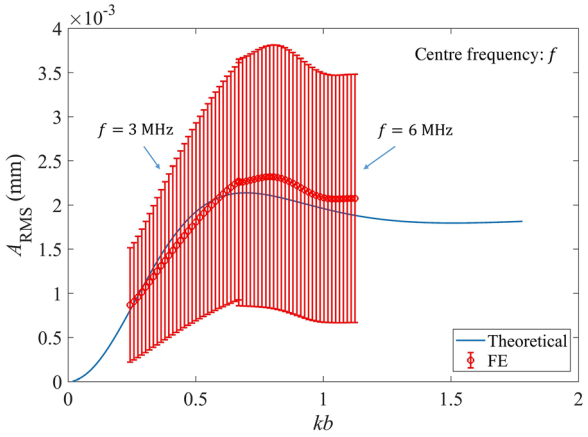



FIG. 5. (Color online) Comparison of FE and theoretical rms backscattering amplitudes of single random shaped grains with a cubic material whose Zener anisotropy factor is 1.4. Five hundred random grains with random orientations for the cubic material are considered as the inclusion at the central axis in the "single-grain" model. The rms of the 500 FE results are plotted as red dots and the error bars show their standard deviation. Two centre frequencies, 3 and 6 MHz, are used in the FE simulations.

Figure 5 shows the comparison of the FE and theoretical predictions, where the $x$ axis shows the product of the wave number $k$ and half of the average linear dimension of the grains in the "multi-grain" model, denoted by $b$ ($b$ is constant at 0.17 mm in Fig. 5). The FE predicted rms backscattering amplitude is plotted as the red dots and their standard deviation is shown with the error bars. Two centre frequencies, 3 and 6 MHz, are used in the FE simulations in order to cover a large range of $kb$, therefore there are two sections of the FE results. The theoretical prediction calculated using Eq. (4) is plotted as the blue curve. The good agreement between the FE and theoretical predictions shows that the implementation of the 3D FE model for the scattering response from single grains is correct and therefore it has strong potential to predict grain noise, as discussed in Secs. III and IV. Discrepancies up to 10% can be seen in the FE results compared to the ISM predictions. A possible reason for this difference is that 500 realisations are not sufficient; however, a compromise has to be made between the accuracy and computational time.

## III. PREDICTION OF GRAIN NOISE MEASURED WITH PLANE WAVE EXCITATION AND POINT RECEIVERS

In this section, the grain noise generated with plane wave excitation will be investigated. A theoretical model will be developed following the derivation of the ISM in Margetan *et al.* (1993) and the noise predicted by the model will be compared with that given by the 3D FE approach verified in Sec. II. The capability of 3D FE to model the physics of wave scattering in polycrystals has been proved in recent FE modelling papers (Van Pamel *et al.*, 2015; Van Pamel *et al.*, 2016; Van Pamel *et al.*, 2018; Van Pamel *et al.*, 2017) and this paper introduces a new application of it to the backscatter problem. Therefore, the adaptation of the ISM to the case studied in this paper and comparing the FE result with this theoretical prediction was done to verify the implementation of the FE model, rather than to validate the FE

approach. Although the ISM is not the up-to-date model in this field, it is simple and has been experimentally validated to give accurate noise prediction within the range of validity, so it is used here; it is clear that the FE results will depart from the analytical solution at lower *kb* values than from the double scatterer model, but since the aim was to check the implementation rather than repeat the model validation of Van Pamel *et al.* (2015), Van Pamel *et al.* (2016), Van Pamel *et al.* (2018), and Van Pamel *et al.* (2017), this was deemed sufficient.

We will start with the development of the adapted theoretical model. The assumptions adopted during the derivation are:

(1) Only longitudinal-to-longitudinal wave scattering is considered.
(2) There is no multiple scattering phenomenon, i.e., the reflection from one grain is not affected by other grains.
(3) Total grain noise is the incoherent sum of the reflections from single grains, i.e., the phases of the individual reflections are not correlated.
(4) No attenuation is considered, which is a direct consequence of assumption 2 above that stipulates that the reflection from one grain is not affected by other grains. This is different from the ISM (Margetan *et al.*, 1993), which included attenuation in the derivation.
(5) As the configuration with a plane wave excitation and point receivers is adopted, considering the duration of the excitation pulse, the reflections arriving at a given time instant are from the grains in between two paraboloid surfaces. Here for computational convenience, the surfaces are only approximated as hemispherical surfaces, i.e., the grains contributing to the grain noise at a given time instant are located in between two hemispherical surfaces. As a result of this approximation, the $N_{\mathrm{RMS}}(t)$ calculated in Eq. (15) is actually independent of time $t$.
(6) Only the normal component of the received displacement contributes to the received signal. This assumption is made to enable a direct comparison with the FE result, which is also captured in the backward direction.
(7) The directionality of the scattering from the grain within the narrow receiving angle of the transducer is neglected.

In connection with assumption 4 above, we should point out that studies (Margetan *et al.*, 1993; Nagy and Adler, 1988; Nagy *et al.*, 1987) have found that the attenuation coefficient determined by the decay of grain noise is significantly less than that determined by coherent frontwall and backwall signals. A modified attenuation coefficient weighted by a forward-scattering factor was introduced by Weaver (1990) that accounts for the reduced attenuation observed in the early part of incoherent grain backscattering and recent analytical models treat this reduced attenuation as a fitting parameter. However, as our purpose was to demonstrate that the FE simulation results asymptotically approach the theoretical predictions in the weak scattering approximation where scattering induced attenuation is weak, ignoring this attenuation is reasonable. Furthermore, in some cases shown in Margetan *et al.* (1993), the attenuation coefficients deduced by the depth dependence of the grain noise are close to zero, which also indicates that it is reasonable to adopt this assumption in our theoretical model.

There is no surprise that if the assumptions break down, a discrepancy will be seen. However, observing the discrepancy and understanding the reason for it is still helpful to have a good understanding of the FE result.

Consider a 3D model with an infinite width. The points on one of the model surfaces, referred to as the transmitting and receiving plane in Fig. 6, are used to transmit a plane wave excitation into the model (in the normal direction) and receive the reflected signals. According to assumption 3, we first calculate the reflection received by a point receiver from a single grain in the model and then sum the reflections from all the grains to obtain the total grain noise observed at the receiver. Finally, the rms of the noise received at different point receivers is discussed.

Assume all the transmitters are excited by a toneburst

$$u_0(t) = E(t)\mathrm{e}^{\mathrm{j}\omega t}, \tag{6}$$

where $E(t)$ is the envelope function of the excitation signal, whose peak amplitude is unity, $\omega$ is the angular frequency, and $t$ is time.

Consider the reflection from a grain with an index of $i$. This grain is located at $(r_i, \theta_i, \varphi_i)$ in the spherical coordinate system. According to assumptions 6 and 7, the amplitude of the reflection from this grain received by one of the point receivers located at the origin can be written as

$$u_{\mathrm{s}}(t, r_i, \theta_i, \varphi_i) = \frac{A_i \cos(\theta_i) E(t - t_{0i})\mathrm{e}^{\mathrm{j}\omega(t-t_{0i})}}{r_i}, \tag{7}$$

where $t_{0i} = 2r_i/v$, (according to assumption 5, where $v$ is the longitudinal velocity), $A_i$ is the L-L backscattering amplitude from the grain, and the meanings of other symbols are shown in Fig. 6. The cos function is introduced to account for the angle of incidence of the scattered wave at the location of the point receiver, as it is assumed that only the normal component of the received displacement contributes to the received signal.

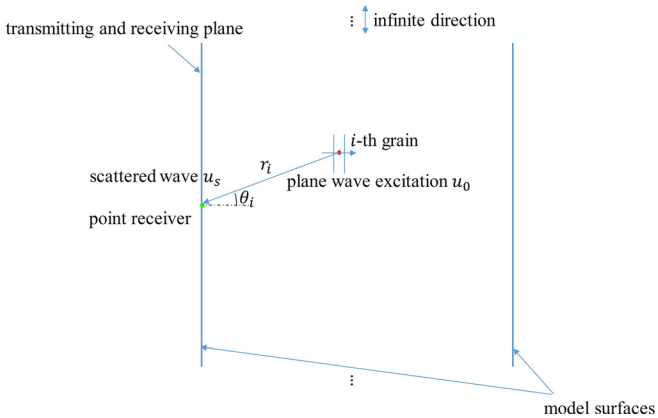



FIG. 6. (Color online) A schematic of a 2D section of the 3D theoretical model used for grain noise prediction with the plane wave configuration.

For convenience, Eq. (7) can be rewritten as

$$u_s(t, r_i, \theta_i, \varphi_i) = B_i e^{j\omega(t-t_{0i})}, \tag{8}$$

where

$$B_i = \frac{A_i \cos(\theta_i) E(t - t_{0i})}{r_i}. \tag{9}$$

Under assumptions 2 and 3, the grain noise received by the point receiver at a given time instant is the sum of the reflections from individual grains arriving at the receiver at that time instant (Margetan *et al.*, 1993)

$$u(t) = \sum_{i=1}^{m} u_s(t, r_i, \theta_i, \varphi_i). \tag{10}$$

Compared with coherent averaging, incoherent averaging enables more information of the grain noise to be shown in the averaged signals, rather than cancelled out during the averaging. Therefore, here, instead of the mean of the received signals, the rms of them will be used to quantify the grain noise level. As it is understood that the physical value of the reflection amplitude is the real part of its complex counterpart (Margetan *et al.*, 1993), the normalised rms of the noise received by multiple point receivers is defined as

$$N_{\mathrm{RMS}}(t) = \sqrt{\langle \mathrm{Re}^2(u(t)) \rangle}, \tag{11}$$

where $\langle\,\rangle$ denotes the average over all the point receivers on the transmitting and receiving plane

According to Margetan *et al.* (1993)

$$\langle \mathrm{Re}^2(u(t)) \rangle = \frac{1}{2} \sum_{i=1}^{m} \langle |B_i|^2 \rangle. \tag{12}$$

Substituting Eq. (9) into Eq. (12) and replacing the sum over grains by an integral over the volume of the model

$$\langle \mathrm{Re}^2(u(t)) \rangle = \frac{1}{2} n_g \langle |A_i|^2 \rangle \times \int\int\int \frac{\cos^2(\theta) E^2(t - t_0)}{r^2} r^2 \sin(\theta) \mathrm{d}r \mathrm{d}\theta \mathrm{d}\varphi, \tag{13}$$

where $t = 2r/v$.

According to assumption 5, the grains contributing to the grain noise at a given time instant are located in between two hemispherical surfaces with radii of $r_1$ and $r_2$. This assumption is not accurate at a large reflection angle $\theta$. However, due to assumption 6, the main contribution to the noise comes from the grains located at a relatively small reflection angle $\theta$, which makes this simplification applicable. In this case, Eq. (13) can be rewritten as

$$\langle \mathrm{Re}^2(u(t)) \rangle = \frac{1}{2} n_g \langle |A_i|^2 \rangle \int_0^{2\pi} \mathrm{d}\varphi \int_0^{\pi/2} \cos^2(\theta) \sin(\theta) \mathrm{d}\theta \times \int_{r_1}^{r_2} E^2(t - t_0) \mathrm{d}r. \tag{14}$$

Substituting Eq. (14) into Eq. (11), $N_{\mathrm{RMS}}(t)$ can be expressed as

$$N_{\mathrm{RMS}}(t) = \sqrt{n_g} A_{\mathrm{RMS}} \sqrt{\frac{\pi}{3} \int_{r_1}^{r_2} E^2(t - t_0) \mathrm{d}r}, \tag{15}$$

where $A_{\mathrm{RMS}} = \sqrt{\langle |A_i|^2 \rangle}$ and can be obtained using Eq. (4). The choice of time origin in Eq. (15) is arbitrary. Here, it is chosen as the centre of the excitation signal, which means that $r_1 = v(t + \tau_1)/2$ and $r_2 = v(t + \tau_2)/2$, where $\tau$ is a time coordinate which is defined to be zero at the centre of the excitation signal and the envelope function of the excitation signal is non-zero between $\tau_1$ and $\tau_2$. In this case, Eq. (15) can be expressed as

$$N_{\mathrm{RMS}}(t) = \sqrt{n_g} A_{\mathrm{RMS}} \sqrt{\frac{v\pi}{6} \int_{\tau_1}^{\tau_2} E^2(\tau) \mathrm{d}\tau}. \tag{16}$$

From Eq. (16), it can be seen that without the attenuation, the noise rms is independent of time. This is because, although the reflection from single grains at larger depth is smaller than their counterparts close to the receiver, the total number of grains increases with depth, which compensates for the decrease of the contribution from single grains.

Next, we will use the 3D FE approach to predict the normalised noise rms and compare the results with the theoretical predictions. Another "multi-grain" model, which has dimensions of $13 \times 13 \times 50\,\mathrm{mm}^3$ and contains 67 600 grains (with an average linear dimension of 0.34 mm), will be used in the FE simulations.

As shown in Fig. 7, symmetry boundary conditions, which have been argued to be an acceptable approximation in Van Pamel *et al.* (2017), are used on all the model surfaces parallel to the $z$ direction; one of the model surfaces on the $x$–$y$ plane is used as the transmitting plane, where all the nodes are sending a 3-cycle Hann-windowed force toneburst into the model [For a Hann window with the peak amplitude of 1, $\int_{\tau_1}^{\tau_2} E^2(\tau)\mathrm{d}\tau$ in Eq. (16) is $3(\tau_2 - \tau_1)/8$], thereby producing a plane wave excitation propagating in the $z$ direction; the same nodes are also used as receivers to measure the grain noise. For each case discussed in this section, five realisations with random crystallographic orientations of the model are run. In each realisation, an incoherent average (rms) is taken over the signals received by all the receivers. Then the rms of the five incoherently averaged signals will be used for discussion. This configuration represents a

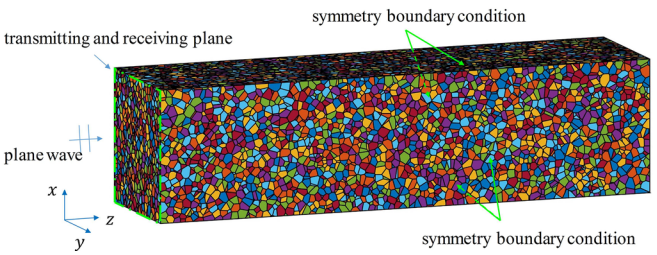



FIG. 7. (Color online) Multi-grain model ($13 \times 13 \times 50\,\mathrm{mm}^3$) with plane wave excitation. Point transmitters/receivers are uniformly distributed on the transmitting and receiving plane.

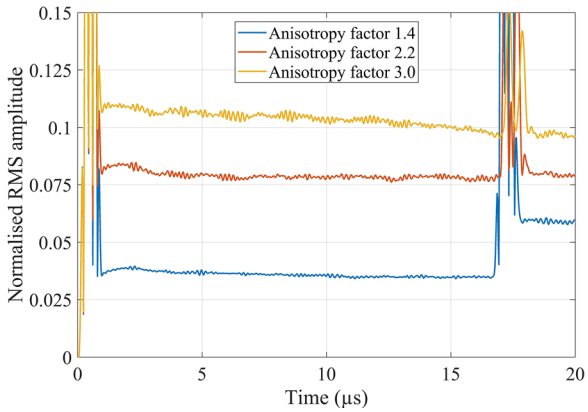



FIG. 8. (Color online) Spatial rms of signals received by all the point receivers. The centre frequency of the excitation is 3 MHz. Three anisotropy factors, 1.4, 2.2, and 3.0, are discussed here. The frontwalls and backwalls are clipped where needed to highlight the grain noise.

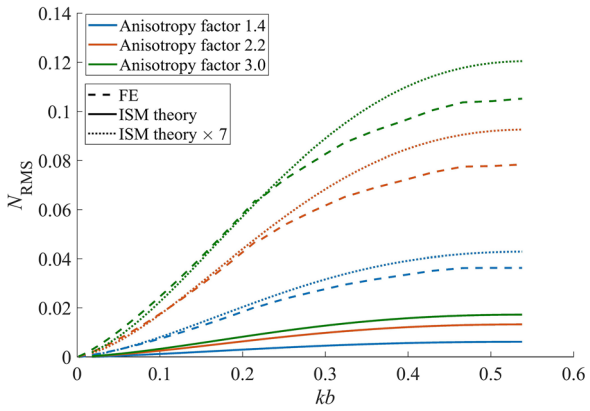



FIG. 9. (Color online) Comparison of FE, theoretical noise rms, and sevenfold theoretical noise rms. The points on the dashed lines are the rms noise (as shown in Fig. 8) within a rectangular time window between 5 and 8 $\mu$s at different centre frequencies.

phase-insensitive measurement of the backscattered incoherent ultrasonic field (Johnston and Miller, 1986).

Figure 8 shows the rms signals under a 3 MHz excitation. Three cubic materials are considered. They have the same density, Poisson's ratio and longitudinal wave speed calculated by the Voigt approximation, as 8000 kg/m$^3$, 0.3, and 6000 m/s, respectively, but a different degree of anisotropy, which is described by the Zener anisotropy factor $A_z$ (Lau and McCurdy, 1998) here. The elastic constants of the materials are listed in Table I, along with their Zener anisotropy factors, which will be used to refer to the materials. To highlight the grain noise, the frontwalls and backwalls are clipped in the figure. It can be seen that a higher noise level can be observed with a higher anisotropy factor. In addition, it is observed that with relatively low anisotropy factors, 1.4 and 2.2, the grain noise is independent of time, which is consistent with the theoretical solution, while with a relatively high anisotropy factor, 3.0, the noise decreases with time, which indicates that scattering induced attenuation occurs. The scattering induced attenuation is inherently a multiple scattering effect, as under the single scattering approximation, backscattering from any given scatterer is not affected by scattering from other scatterers. However, as mentioned earlier, the theoretical model ignores multiple scattering effects and predicts a noise level constant with time. Therefore, the FE results received in an early time range, from 5 to 8 $\mu$s, which is less affected by the scattering induced attenuation, will be used later for comparison with the theoretical predictions.

Figure 9 shows the comparison of the FE and theoretically predicted noise rms. The centre frequency used in the FE simulations is in the range from 0.6 to 3 MHz. The blue, red, and green curves show the predictions of cubic materials with anisotropy factors of 1.4, 2.2, and 3.0. The theoretical predictions are plotted as the solid curves and the FE results are shown as dashed curves. The points on the dashed lines are the rms noise, as shown in Fig. 8, within a rectangular time window between 5 and 8 $\mu$s (to reduce multiple scattering effects, as mentioned above) at different centre frequencies. From the figure, a big discrepancy between the two predictions can be seen and significantly higher backscattering is observed in the FE predictions. After multiplying the theoretical results by seven (the dotted line), relatively good agreement can be seen, which shows that the FE results indicate a similar frequency dependence to the theoretical predictions.

A possible reason for this discrepancy is the contribution of shear waves, which is not accounted for in the theoretical model, but is implicitly captured in the FE simulations. This contribution can be particularly strong when the shear wave reflection hits a point receiver at an oblique angle, as shown in Fig. 10. It is to be expected that shear waves would be the dominant component of the noise seen by a point receiver, as without spatial filtering, each point receiver acts as a phase-insensitive device that essentially measures the incident energy (Nagy *et al.*, 1987), and both theoretical and experimental studies have shown that in the Rayleigh regime about 80% of the energy in an incident longitudinal wave is scattered as shear waves (Papadakis, 1981).

As can be inferred from Fig. 10, the shear waves incident at oblique angles will be cancelled out quickly by taking a coherent average over the receiving plane, since the phase varies rapidly over the receiver face. Figure 11 shows the relationship between the noise rms and the edge length of a square coherent averaging area (expressed in shear

TABLE I. Elastic constants and anisotropy factors of the cubic materials discussed in this section.

| $C_{11}$ (GPa) | $C_{12}$ (GPa) | $C_{44}$ (GPa) | $A_z = 2C_{44}/(C_{11} - C_{12})$ (Lau and McCurdy, 1998) |
|---|---|---|---|
| 266.8 | 134.0 | 92.9 | 1.4 |
| 242.0 | 146.4 | 105.3 | 2.2 |
| 228.1 | 153.4 | 112.2 | 3.0 |

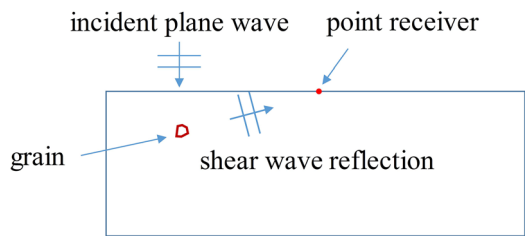



FIG. 10. (Color online) A schematic showing how a shear wave contributes to a signal received at a point receiver.

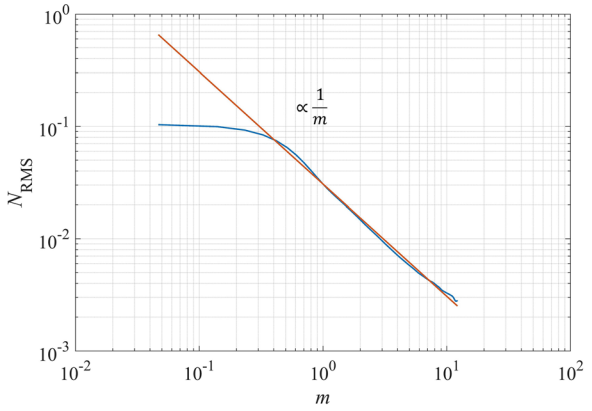



FIG. 11. (Color online) Noise rms vs edge length of the square coherent averaging area (expressed in shear wavelengths and denoted by $m$). Each point on the blue curve is obtained in a similar way as that used to plot Fig. 9, except that the spatial rms is taken over the signals obtained by coherently averaging the signals on areas with dimensions of $m \times m$ wavelength square across the receiving plane. The red line is proportional to $1/m$.

wavelengths and denoted by $m$). Each point on the blue curve is obtained in a similar way as that used to plot Fig. 9, except that the spatial rms is no longer taken over the signals received by the point receivers, but is taken over the signals obtained by coherently averaging the received signals on areas with dimensions of $m \times m$ wavelength square across the receiving plane. This simulates the signals received by a transducer with the same dimensions at different locations (i.e., different locations of a $m \times m$ wavelength square transducer are simulated and the rms of the signals obtained at the different transducer locations is taken). It can be seen that the noise rms drops rapidly after the edge length of the coherent averaging area reaches the shear wavelength. Some of this effect could be due to the cancellation of longitudinal waves. However, the oblique longitudinal waves are relatively weak as longitudinal scattering is stronger close to the normal direction, and the longitudinal waves are slower to cancel as their wavelength is longer than the shear wavelength. Therefore, the decrease of the noise rms is mainly due to the cancellation of the shear waves, which indicates that oblique shear waves are a significant contributor to the noise seen by a point receiver and so explains the discrepancy between the FE results and the analytical solution for L-L scattering with point receivers, shown in Fig. 9. It can also be seen from Fig. 11 that the noise rms decreases with $1/m$, as indicated by the red line, rather than $1/\sqrt{m}$, which is because the coherent averaging is over a 2D surface rather than a line.

## IV. PREDICTION OF GRAIN NOISE MEASURED WITH A FINITE TRANSDUCER

Having discussed a basic configuration, in which the grain noise is excited by a plane wave and received by individual point receivers, in this section, we will investigate a more practical configuration with a finite contact transducer, and predict the grain noise that it generates and receives. This section will follow a similar procedure to that described in the last section. First, a theoretical model predicting the grain noise level will be given and then the result will be compared with that obtained by FE, where the contribution of shear waves and multiple scattering will be discussed.

We will start with a brief introduction of how to establish the theoretical model using a similar procedure to that used in Margetan *et al.* (1994). During the derivation, all the assumptions mentioned in the last section, except assumption 5, are adopted and it is also assumed that the grains are small compared to the beam diameter, in which case, the excitation incident on each grain can be regarded as a quasi-plane wave.

In Margetan *et al.* (1994), the Thompson and Gray (1983) model, which was developed for rigid piston transducers, was used to calculate the reflection coefficients from single grains. According to Schmerr and Sedov (1996), this model can be used without any modification for apodized transducers if the apodization is the same in transmission and reception, which is the case that we consider in this section. Therefore, the normalised change of the displacement received by an apodized transducer induced by a grain located at $(x_i, y_i, z_i)$ can be expressed as

$$\delta\Gamma_s(\omega, x_i, y_i, z_i) = \frac{2V^2(\omega, x_i, y_i, z_i)}{V_0^2} \frac{A_i(\omega)}{\mathrm{j}k(\omega)a^2}, \tag{17}$$

where $a$, $\rho$, $v$, $A_i$, $k$ denote transducer radius, medium density, longitudinal wave speed, backscattering amplitude of the grain and wave number. $V$ is the peak particle velocity at the location of the grain. $V_0$ is the peak velocity amplitude at the centre of the transducer.

Assume the transducer is excited by a toneburst $S_0(t) = E(t)\mathrm{e}^{\mathrm{j}\omega_0 t}$. The peak amplitude of $E(t)$ is unity and the Fourier transform of $S_0(t)$ is denoted by $U_0(\omega)$. The reflection signal in the frequency domain can be expressed as

$$\delta U_s(\omega, x_i, y_i, z_i) = \delta\Gamma_s(\omega, x_i, y_i, z_i) U_0(\omega). \tag{18}$$

In the time domain, it is denoted by $\delta S_s(t + t_{0i}, x_i, y_i, z_i))$, where $t_{0i} = 2z_i/v$. If we replace $t + t_{0i}$ with $t$ and collect all the constants and functions, which are slowly varying with $\omega$ into a term $H$ and evaluated at $\omega = \omega_0$, $\delta S_s$ can be written as

$$\begin{aligned}\delta S_s(t, x_i, y_i, z_i) &= H(\omega_0, x_i, y_i, z_i) \frac{1}{2\pi} \int_{-\infty}^{\infty} U_0(\omega)\mathrm{e}^{\mathrm{j}\omega t}\mathrm{d}\omega \\ &= H(\omega_0, x_i, y_i, z_i) E(t - t_{0i})\mathrm{e}^{\mathrm{j}\omega_0(t - t_{0i})},\end{aligned} \tag{19}$$

where

$$H(\omega_0, x_i, y_i, z_i) = \frac{2V^2(\omega_0, x_i, y_i, z_i)}{V_0^2} \frac{A_i(\omega_0)}{\mathrm{j}k(\omega_0)a^2}. \tag{20}$$

From Eq. (20), we follow a similar procedure with that used in Margetan *et al.* (1994) and obtain

$$\begin{aligned}N_{\mathrm{RMS}}(t) = \sqrt{2n_g} \frac{A_{\mathrm{RMS}}(\omega_0)}{V_0^2 k(\omega_0)a^2} \\ \times \sqrt{\int\int\int |V^4(\omega_0, x, y, z)| E^2(t - t_0)\mathrm{d}x\mathrm{d}y\mathrm{d}z}.\end{aligned} \tag{21}$$

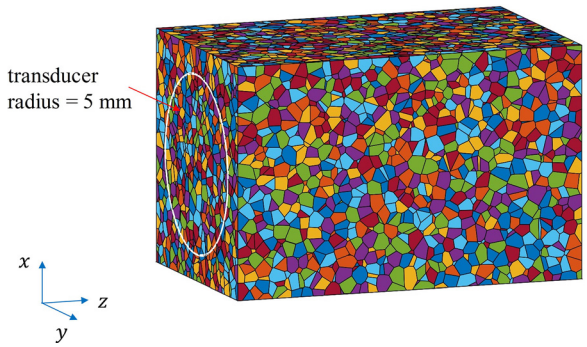



FIG. 12. (Color online) "Multi-grain" model ($13 \times 13 \times 20\,\text{mm}^3$). A 5 mm radius focused transducer is outlined by the white circle. Focusing is achieved through adding time delays to the excitation and reception of individual nodes. A Hann-window is applied on the excitation amplitude over the plane of the transducer to remove surface waves.

Equation (21) can be simplified by introducing

$$G(\omega_0, z) = \left| \int\int V^4(\omega_0, x, y, z)\mathrm{d}x\mathrm{d}y \right|. \tag{22}$$

Similar to Sec. III, Eq. (21) can be rewritten as

$$N_{\mathrm{RMS}}(t) = \sqrt{n_g v}\frac{A_{\mathrm{RMS}}(\omega_0)}{V_0^2 k(\omega_0)a^2} \times \sqrt{\int_{\tau_1}^{\tau_2} G\left(\omega_0, \frac{v(t+\tau)}{2}\right)E^2(\tau)\mathrm{d}\tau}. \tag{23}$$

The $G[\omega_0, v(t+\tau)/2]$ required in Eq. (23) can be approximated by a Gaussian model or a Gauss-Hermite model (Margetan *et al.*, 1993), or obtained by a FE simulation, as discussed in the following example.

Next, an example case will be given to compare the grain noise predicted with the theoretical model described above and the FE approach. A focused contact transducer, which has a radius of 5 mm and an actual focal length of 6 mm, is used, exciting the testpiece with a 3-cycle Hann-windowed force toneburst, of which the centre frequency is 4 MHz. The amplitude distribution of the excitation across the transducer surface follows a 2D Hann-window. The cubic materials listed in Table I will be used.

As a comparison of the theoretical and FE predictions will be carried out, the peak amplitude of the velocity excitation at the centre of the transducer [$V_0$ in Eq. (21)] and the velocity field [$V(\omega_0, x, y, z)$ in Eq. (21)] used for theoretical noise calculation will be measured with FE to ensure that the same excitation and wave field are considered.

The multi-grain model used in the FE simulations is shown in Fig. 12. The white circle outlines the focused transducer, where focusing is achieved through adding time delays to the excitation and reception of individual nodes. Symmetry boundary conditions are used on all the surfaces normal to the transducer plane. For each case discussed in this section, 50 realisations with random crystallographic orientations of the model are run. For the sake of computational efficiency, the tessellation of the grain structure is kept the same (Van Pamel *et al.*, 2017). In each realisation, a coherent average over the transducer surface is taken, simulating a signal received by the transducer at one position. Then the rms signal of the 50 averaged signals is used for comparison with the theoretical prediction.

The FE predicted grain noise is plotted as the blue curves in Fig. 13, along with the theoretical predictions, shown as the red curves, and relative errors (theoretical noise—FE noise)/theoretical noise), shown as the green dashed curves with the right-hand $y$ axis scale. Figure 13(a), where the anisotropy factor is 1.4, shows very good agreement. However, relatively large discrepancies can be seen in Figs. 13(b) and 13(c) with anisotropy factors of 2.2 and 3.0, where the peaks caused by focusing in the FE predictions appear at earlier times than those in the theoretical curves. This is because the peak of the noise predicted by FE shifts to an earlier time with a higher anisotropy factor, while that given by the ISM theory is independent of anisotropy factor. The discrepancies of noise levels are dependent on time (or depth), indicating that this is caused by the scattering induced attenuation, which is not accounted for in the theoretical model.

To test whether the scattering induced attenuation is the reason for the discrepancies, the theoretical solution was multiplied by an attenuation term. The attenuation term follows an exponential function $\exp(-2\alpha z)$, where $z$ is depth and $\alpha$ is attenuation coefficient, which is deduced by comparing the amplitude of the average of the backwall reflection to that of the excitation obtained in Sec. III with the plane wave model. As the attenuation term is determined by coherent echoes, it is referred to as coherent attenuation. The unattenuated and attenuated theoretical predictions are compared with the FE results using a dB scale in Fig. 14. It can be seen

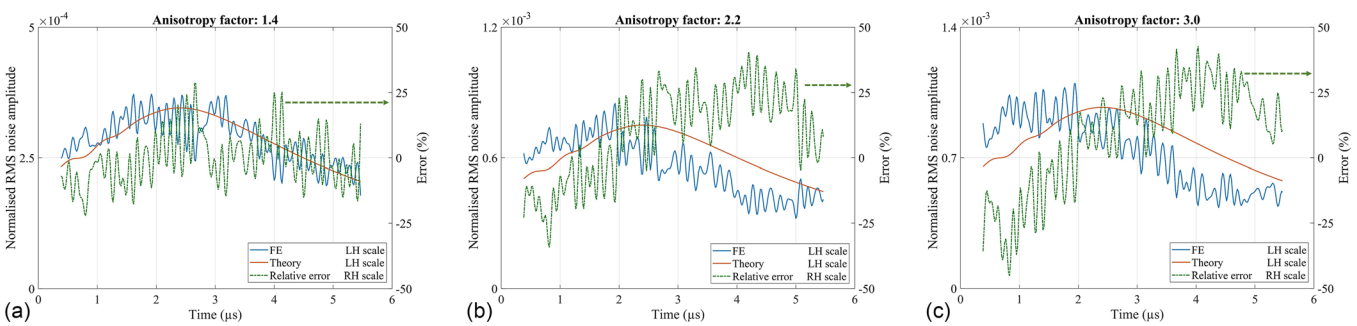



FIG. 13. (Color online) Comparison of FE and theoretical grain noise obtained with a contact-focused transducer with anisotropy factors of (a) 1.4, (b) 2.2, and (c) 3.0. The green lines show the relative error to the theoretical predictions. Attenuation of noise is not taken into account in the theory.

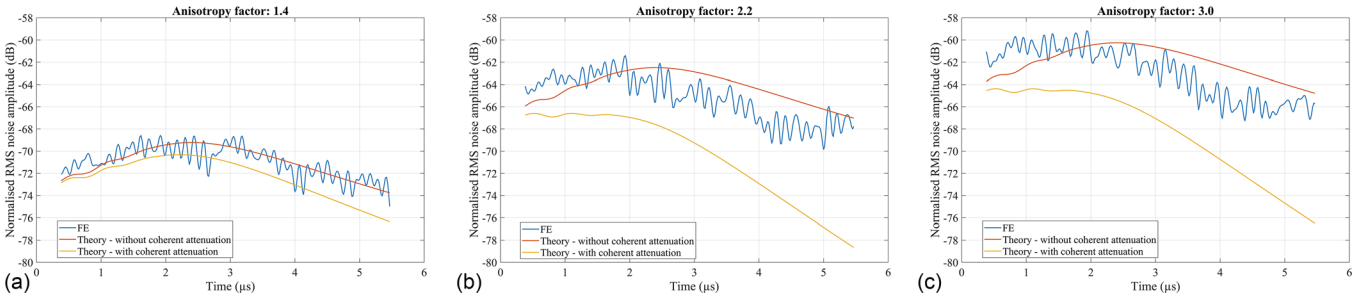



FIG. 14. (Color online) Comparison of theoretical grain noise with and without coherent attenuation and FE results. The anisotropy factors are (a) 1.4, (b) 2.2, and (c) 3.0, respectively. Coherent attenuation is considered by multiplying the theoretical solution by an attenuation term $\exp(-2\alpha z)$, where $z$ is depth and $\alpha$ is attenuation coefficient, which is deduced by comparing the amplitude of the average of the backwall reflection to that of the excitation obtained in Sec. III with the plane wave model.

that attenuation decreases the noise levels more significantly at a later time, as expected. When the anisotropy factor is 2.2 and 3.0, it smooths out the peak around the focal point. This makes the curves more similar to the FE results than the unattenuated solutions, which indicates the discrepancies could be due to the attenuation. However, it can also be seen that the attenuated theoretical solutions are significantly lower than the FE results. This means that the scattering induced attenuation has a more significant influence on the coherent waves than the grain noise, so the attenuation coefficient deduced using the coherent waves is much higher than that deduced by the incoherent noise, which has been reported in Margetan *et al.* (1993), Nagy and Adler (1988), and Nagy *et al.* (1987).

In this section, the grain noise excited and captured by a finite contact transducer has been predicted with the adapted theoretical model and the FE approach, the contributions of shear waves and multiple scattering being included in the FE analysis but not in the analytical solution. From the results shown in Fig. 13(a), good agreement between the unattenuated theoretical prediction and the FE result can be seen, which implies that the contribution of shear waves is negligible, as expected due to the spatial averaging over the transducer surface, and multiple scattering has little influence on the grain noise level, as the anisotropy factor is relatively low and the backscattering is weak. However, with relatively high anisotropy factors, discrepancies are observed in Figs. 13(b) and 13(c), indicating the occurrence of multiple scattering. In conclusion, good agreement between the FE and theoretical noise predictions can be seen in the weakly scattering case; the discrepancies seen in the highly scattering cases demonstrate that FE is attractive in describing the backscattering noise behaviour as it does not involve some of the important simplifying assumptions included in the theoretical model and therefore is able to capture multiple scattering which is ignored in the theory.

## V. CONCLUSIONS

Theories describing the ultrasonic backscattered noise behaviour in polycrystalline materials have been widely researched. Most of them are based on a single scattering assumption, which limits their application. In this paper, an alternative 3D FE approach, which can solve the scattering problem without major simplifying assumptions and so has the potential of overcoming the limitations, has been presented. It has been used to predict the longitudinal-to-longitudinal backscattering amplitudes from single grains and the rms noise levels with different transmit-receive configurations. By comparing the FE predictions with those given by the existing theoretical models, the main conclusions are:

(1) The 3D FE results of the rms of L-L backscattering amplitudes from single grains agree well with the theoretical predictions. The maximum discrepancy between the FE and theoretical predictions of the rms backscattering amplitude of single random grains is around 10% in the case discussed in Sec. II C.
(2) With a transmit-receive configuration of a plane wave excitation and point receivers, which represents a phase-insensitive measurement of the backscattered incoherent ultrasonic field, FE gives a significantly higher noise prediction than the ISM solution. The shear wave component is expected to be a major factor for the difference, but the investigation of this is left as a challenge for the future.
(3) With a finite transducer, the FE predicted noise level agrees well with that given by the ISM theory when the scattering is relatively weak. When the scattering is relatively high, discrepancies are seen between the FE and theoretical results, which is largely due to multiple scattering, which is only accounted for in the FE simulations but not in the theory.

Therefore, good agreement between the 3D FE and theoretical noise predictions can be seen when the scattering is relatively weak so that it is within the validity of the ISM theory. 3D FE can implicitly capture longitudinal-to-transverse scattering and multiple scattering, which enables it to be used for phase-insensitive scattering problems and highly scattering problems. As computer power increases, 3D finite element analysis is likely to find increasing application and to further our understanding of elastic wave propagation and scattering in polycrystalline materials.

## ACKNOWLEDGMENTS

This work was partially supported by EPSRC via the UK Research Centre in NDE Grant No. EP/L022125/1. The authors are grateful to Dr. Peter Huthwaite, the author of the POGO software that was used, and Professor Mike Lowe for

helpful discussions. Y.L. would like to thank the China Scholarship Council for personal funding in the form of a Ph.D. scholarship.

Ahmed, S., and Thompson, R. B. (**1996**). "Propagation of elastic waves in equiaxed stainless-steel polycrystals with aligned [001] axes," J. Acoust. Soc. Am. **99**, 2086–2096.

Arguelles, A. P., Kube, C. M., Hu, P., and Turner, J. A. (**2016**). "Mode-converted ultrasonic scattering in polycrystals with elongated grains," J. Acoust. Soc. Am. **140**, 1570–1580.

Bai, X., Tie, B., Schmitt, J. H., and Aubry, D. (**2018**). "Finite element modeling of grain size effects on the ultrasonicmicrostructural noise backscattering in polycrystalline materials," Ultrasonics **87**, 182–202.

Chassignole, B., Duwig, V., Ploix, M.-A., Guy, P., and El Guerjouma, R. (**2009**). "Modelling the attenuation in the athena finite elements code for the ultrasonic testing of austenitic stainless steel welds," Ultrasonics **49**, 653–658.

Drozdz, M. B. (**2008**). "Efficient finite element modelling of ultrasound waves in elastic media," Ph.D. thesis, Imperial College London, London, UK.

Feuilly, N., Dupond, O., Chassignole, B., Moysan, J., and Comeloup, G. (**2009**). "Relation between ultrasonic backscattering and microstructure for polycrystalline materials," AIP Conf. Proc. **1096**, 1216–1223.

Ghoshal, G., and Turner, J. A. (**2009**). "Diffuse ultrasonic backscatter in a two-dimensional domain," Acta Mech. **205**, 35–49.

Ghoshal, G., and Turner, J. A. (**2010**). "Diffuse ultrasonic backscatter at normal incidence through a curved interface," J. Acoust. Soc. Am. **128**, 3449–3458.

Ghoshal, G., Turner, J. A., and Weaver, R. L. (**2007**). "Wigner distribution of a transducer beam pattern within a multiple scattering formalism for heterogeneous solids," J. Acoust. Soc. Am. **122**, 2009–2021.

Gubernatis, J., Domany, E., Krumhansl, J., and Huberman, M. (**1977**). "The born approximation in the theory of the scattering of elastic waves by flaws," J. Appl. Phys. **48**, 2812–2819.

Han, Y. K., and Thompson, R. B. (**1997**). "Ultrasonic backscattering in duplex microstructures: Theory and application to titanium alloys," Metallur. Mater. Trans. A **28**, 91–104.

Hu, P., Kube, C. M., Koester, L. W., and Turner, J. A. (**2013**). "Mode-converted diffuse ultrasonic backscatter," J. Acoust. Soc. Am. **134**, 982–990.

Hu, P., and Turner, J. A. (**2015**). "Contribution of double scattering in diffuse ultrasonic backscatter measurements," J. Acoust. Soc. Am. **137**, 321–334.

Hu, P., and Turner, J. A. (**2017**). "Transverse-to-transverse diffuse ultrasonic scattering," J. Acoust. Soc. Am. **142**, 1112–1120.

Huthwaite, P. (**2014**). "Accelerated finite element elastodynamic simulations using the GPU," J. Comput. Phys. **257**, 687–707.

Johnston, P. H., and Miller, J. G. (**1986**). "Phase-insensitive detection for measurement of backscattered ultrasound," IEEE Trans. Ultrason. Ferroelectr. Freq. Control **33**, 713–721.

Lau, K., and McCurdy, A. K. (**1998**). "Elastic anisotropy factors for orthorhombic, tetragonal, and hexagonal crystals," Phys. Rev. B **58**, 8980–8984.

Lobkis, O., Yang, L., Li, J., and Rokhlin, S. (**2012**). "Ultrasonic backscattering in polycrystals with elongated single phase and duplex microstructures," Ultrasonics **52**, 694–705.

Margetan, F. J., Gray, T. A., and Thompson, R. B. (**1991**). "A technique for quantitatively measuring microstructurally induced ultrasonic noise," in *Review of Progress in Quantitative Nondestructive Evaluation* (Springer, New York), Vol. 10B, pp. 1721–1728.

Margetan, F. J., Haldipur, P., Yu, L., and Thompson, R. B. (**2005**). "Looking for multiple scattering effects in backscattered ultrasonic grain noise from jet-engine nickel alloys," AIP Conf. Proc. **760**, 75–82.

Margetan, F. J., Thompson, R. B., and Yalda-Mooshabad, I. (**1994**). "Backscattered microstructural noise in ultrasonic toneburst inspections," J. Nondestruct. Eval. **13**, 111–136.

Margetan, F. J., Thompson, R. B., Yalda-Mooshabad, I., and Han, Y. K. (**1993**). "Detectability of small flaws in advanced engine alloys," Technical Report, Iowa State University, Ames, IA.

Mech, S. J., Michaels, T. E., Emmons, J. S., and Sugiyama, M. M. (**1977**). "Development of ultrasonic examination methods for austenitic stainless steel weld inspection," Technical Report, Hanford Engineering Development Lab., Richland, WA.

Nagy, P. B., and Adler, L. (**1988**). "Scattering induced attenuation of ultrasonic backscattering," in *Review of Progress in Quantitative Nondestructive Evaluation* (Springer, New York), Vol. 7B, pp. 1263–1271.

Nagy, P. B., Rypien, D. V., and Adler, L. (**1987**). "Ultrasonic attenuation measurement by backscattering analysis," in *Review of Progress in Quantitative Nondestructive Evaluation* (Springer, New York), Vol. 6A, pp. 1411–1418.

Papadakis, E. P. (**1981**). "5. scattering in polycrystalline media," in *Methods in Experimental Physics* (Elsevier, Amsterdam, the Netherlands), Vol. 19, pp. 237–298.

Quey, R., Dawson, P. R., and Barbe, F. (**2011**). "Large-scale 3d random polycrystals for the finite element method: Generation, meshing and remeshing," Comput. Methods Appl. Mech. Eng. **200**, 1729–1745.

Rose, J. H. (**1991**). "Ultrasonic backscattering from polycrystalline aggregates using time-domain linear response theory," in *Review of Progress in Quantitative Nondestructive Evaluation* (Springer, New York), Vol. 10B, pp. 1715–1720.

Rose, J. H. (**1992**). "Ultrasonic backscatter from microstructure," in *Review of Progress in Quantitative Nondestructive Evaluation* (Springer, New York), pp. 1677–1684.

Rose, J. H. (**1993**). "Theory of ultrasonic backscatter from multiphase polycrystalline solids," in *Review of Progress in Quantitative Nondestructive Evaluation* (Springer, New York), Vol. 12, pp. 1719–1726.

Ryzy, M., Grabec, T., Sedlák, P., and Veres, I. A. (**2018**). "Influence of grain morphology on ultrasonic wave attenuation in polycrystalline media with statistically equiaxed grains," J. Acoust. Soc. Am. **143**, 219–229.

Schmerr, L. W., and Sedov, A. (**1996**). "Mechanical reciprocity principles and ultrasonic measurement models," in *Review of Progress in Quantitative Nondestructive Evaluation* (Springer, New York), Vol. 15A, pp. 65–71.

Schmerr, L. W., Jr., and Song, J. S. (**2007**). *Ultrasonic Nondestructive Evaluation Systems* (Springer, New York).

Smith, W. D. (**1975**). "The application of finite element analysis to body wave propagation problems," Geophys. J. R. Astronom. Soc. **42**, 747–768.

Stanke, F. E. (**1985**). "Inversion of attenuation measurements in terms of a parameterized autocorrelation function," in *NDE for Microstructure Process Control*, edited by H. N. G. Wadley (American Society for Metals, Materials Park, OH), pp. 55–60.

Stanke, F. E., and Kino, G. S. (**1984**). "A unified theory for elastic wave propagation in polycrystalline materials," J. Acoust. Soc. Am. **75**, 665–681.

Thompson, R. B., and Gray, T. A. (**1983**). "A model relating ultrasonic scattering measurements through liquid–solid interfaces to unbounded medium scattering amplitudes," J. Acoust. Soc. Am. **74**, 1279–1290.

Thompson, R. B., Margetan, F., Han, Y., Paxson, A. J., and Shamblen, C. (**1992**). "Relationship of microstructure to backscattered ultrasonic noise," in *Review of Progress in Quantitative Nondestructive Evaluation* (Springer, New York), Vol. 11, pp. 1685–1691.

Turner, J. A. (**1999**). "Elastic wave propagation and scattering in heterogeneous, anisotropic media: Textured polycrystalline materials," J. Acoust. Soc. Am. **106**, 541–552.

Van Pamel, A., Brett, C. R., Huthwaite, P., and Lowe, M. J. S. (**2015**). "Finite element modelling of elastic wave scattering within a polycrystalline material in two and three dimensions," J. Acoust. Soc. Am. **138**, 2326–2336.

Van Pamel, A., Nagy, P. B., and Lowe, M. J. S. (**2016**). "On the dimensionality of elastic wave scattering within heterogeneous media," J. Acoust. Soc. Am. **140**, 4360–4366.

Van Pamel, A., Sha, G., Lowe, M. J. S., and Rokhlin, S. I. (**2018**). "Numerical and analytic modelling of elastodynamic scattering within polycrystalline materials," J. Acoust. Soc. Am. **143**, 2394–2408.

Van Pamel, A., Sha, G., Rokhlin, S. I., and Lowe, M. J. S. (**2017**). "Finite-element modelling of elastic wave propagation and scattering within heterogeneous media," Proc. R. Soc. A **473**, 20160738.

Weaver, R. L. (**1990**). "Diffusivity of ultrasound in polycrystals," J. Mech. Phys. Solids **38**, 55–86.

Yang, L., Lobkis, O. I., and Rokhlin, S. I. (**2011**). "Explicit model for ultrasonic attenuation in equiaxial hexagonal polycrystalline materials," Ultrasonics **51**, 303–309.

Yang, L., and Rokhlin, S. I. (**2012**). "On comparison of experiment and theory for ultrasonic attenuation in polycrystalline niobium," J. Nondestruct. Eval. **31**, 77–79.

Yang, L., and Rokhlin, S. I. (**2013**). "Ultrasonic backscattering in cubic polycrystals with ellipsoidal grains and texture," J. Nondestruct. Eval. **32**, 142–155.

Ying, C. F., and Truell, R. (**1956**). "Scattering of a plane longitudinal wave by a spherical obstacle in an isotropically elastic solid," J. Appl. Phys. **27**, 1086–1097.